Universiteit Antwerpen

This item is the archived peer-reviewed author-version of:

Use of nanoscale carbon layers on Ag-based gas diffusion electrodes to promote CO production

Reference:
Pacquets Lien, Van den Hoek Järi, Arenas Esteban Daniel, Ciocarlan Radu-George, Cool Pegie, Baert Kitty, Hauffman Tom, Daems Nick, Bals Sara, Breugelmans Tom.- Use of nanoscale carbon layers on Ag-based gas diffusion electrodes to promote CO production
ACS applied nano materials - ISSN 2574-0970 - 5:6(2022), p. 7723-7732
Full text (Publisher's DOI): https://doi.org/10.1021/ACSANM.2C00473
To cite this reference: https://hdl.handle.net/10067/1888870151162165141

uantwerpen.be
Institutional repository IRUA

The Use of Nanoscale Carbon Layers on Ag-Based Gas Diffusion Electrodes to Promote CO Production

*Lien Pacquets[a,b], Järi Van den Hoek[a], Daniel Arenas-Esteban[b], Radu-George Ciocarlan[c], Pegie Cool[c], Kitty Baert[d], Tom Hauffman[d], Nick Daems[a], Sara Bals[b] and Tom Breugelmans[a]**

[a] ELCAT, University of Antwerp, Universiteitsplein 1, 2610 Wilrijk

[b] EMAT, University of Antwerp, Groenenborgerlaan 171, 2020 Antwerpen

[c] LADCA, University of Antwerp, Universiteitsplein 1, 2610 Wilrijk

[d] SURF, Vrije Universiteit Brussel, Pleinlaan 2, 1050 Brussel

*Corresponding authors: tom.breugelmans@uantwerpen.be

KEYWORDS
Stability, gas diffusion electrodes, HER inhibition, nanoscale carbon layer, CO_2 reduction

ABSTRACT
A promising strategy for the inhibition of the hydrogen evolution reaction along with the stabilization of the electrocatalyst in electrochemical CO_2 reduction cells, involves the application of a nanoscale amorphous carbon layer on top of the active catalyst layer in a gas diffusion electrode. Without modifying the chemical nature of the electrocatalyst itself, these amorphous carbon layers lead to the stabilization of the electrocatalyst and a significant improvement with respect to the inhibition of the hydrogen evolution reaction was also obtained. The faradaic efficiencies of hydrogen could be reduced from 31.4 % to 2.1 % after one hour of electrolysis with a 5 nm thick carbon layer. Furthermore, the impact of the carbon layer thickness (5 to 30 nm) on this inhibiting effect was investigated. We determined an optimal thickness of 15 nm where the hydrogen evolution reaction was inhibited and a decent stability was obtained. Next, a thickness of 15 nm was selected for durability measurements. Interestingly, these durability measurements revealed the beneficial impact of the carbon layer already after 6 hours by suppressing the hydrogen evolution such that an increase of only 37.9 % exists compared to 56.9 % without the use of an additional carbon layer, which is an improvement of 150 %. Since the carbon is only applied afterwards, it reveals its great potential in terms of electrocatalysis in general.

1 INTRODUCTION

Electrochemistry is a promising field which allows us to define end products depending on the choice of electrocatalyst and the applied potential. The emerging trend of producing renewable energy, such as solar and wind energy, perfectly fits into the carbon capture and utilization strategy where they strive to covert CO_2 using green energy. Combined, they can become the ideal solution in the battle against climate change.

Therefore, many scientists have devoted their research to electrochemically produce value added products such as methane [1], ethylene [2], CO [3] and formic acid [4] from CO_2. Up until today, the challenge remains to develop a catalyst to efficiently reduce CO_2 by lowering the large overpotential necessary for this reduction, along with the inhibition of the competing hydrogen evolution reaction (HER) and therefore tuning the selectivity in aqueous environments [5]. Various studies have been conducted to suppress the HER by changing catalyst structure [6], alloying catalyst metals [7–11], electrolysis in alkaline media [12,13], reactor design [14], electrode design [14] and catalyst protective layers [15–19]. The latter are often surface modifiers, which primarily aim for changes in selectivity by effectively modifying the electrocatalytic surface properties. Ahn et al. tuned the selectivity of copper (Cu) foam by adsorption of poly-amides and thereby stabilizing the CO dimer which is essential for the formation of C_2 products [16]. Buckley et al. applied organic modifiers on Cu surfaces in order to alter the selectivity between CO, H_2 and formic acid [15]. Hsieh et al. used halide anions at silver (Ag) surfaces influencing the rate-determining step [20]. Recently, researchers started to explore the applications of carbon films and the effect on product distributions, but they mainly focused on higher layer thicknesses [21,22].

In this study, we demonstrate the effect of a nanoscale protective layer, based on amorphous carbon without additional functional groups, on the inhibition of the hydrogen evolution reaction (HER). In contrast to previous studies, the use of a carbon layer doesn't alter the

chemical nature of the electrocatalyst and very importantly, the approach allows us to avoid the use of difficult synthesis methods that add functional groups to tune the product distribution. Additionally, we wanted to explore its stabilizing effect as it could potentially prevent electrocatalyst restructuring.

As a proof of concept, we investigated the effect of the carbon layer and its thickness on Ag-based gas diffusion electrodes (GDEs) for the CO_2 electrochemical reduction to CO. Since Ag is known to produce exclusively CO, it is therefore easier to investigate the influence of the carbon layer on the inhibition of the competitive HER. In addition, by using GDEs as a substrate, the CO_2 can be supplied at the backside, which facilitates the investigating of the HER inhibition. As a next step, the ideal layer thickness was selected to investigate its performance over a longer period of time, revealing the beneficial role of the carbon layer on the durability of Ag-based GDEs. We believe this work can contribute significantly to latest research in the field because of its potential as a catalyst coating serving as a HER inhibitor.

2 EXPERIMENTAL

2.1 Chemicals

Potassium bicarbonate (Chem-Lab, 99,5%), potassium hydroxide (Chem-Lab, 85%), Sigracet® 39BB (SGL Carbon), Selemion® DSVN anion exchange membrane (AEM, AGC Engineering Co., Japan), Nafion 117 (Fuel Cell Store) cation exchange membrane (CEM) were used during this research. All solutions were prepared with ultra-pure water (MQ, Milli-Q grade, 18.2 MΩ cm)

2.2 Electrode preparation

Ag is a well-explored electrocatalyst in literature and is therefore selected for this proof of concept study. Consequently, a 70 nm thick Ag layer was deposited by magnetron sputter coating onto a gas diffusion electrode (GDE, sigracet), using a Leica EM ACE600 employing 35 mA of current, $4.0 .10^{-2}$ mbar of argon (Ar) pressure. Subsequently, a nanoscale carbon layer was added by pulse mode evaporation with thicknesses varying between 0 nm and 30

nm referred to as Ag70Cx (with x indicating the carbon layer thickness on top of the Ag-based GDE) in all experiments (a schematic representation of the synthesis approach and photographs of the different samples can be found in Scheme 1 and Figure S1, respectively). The source was angled 25° towards the sample stage.

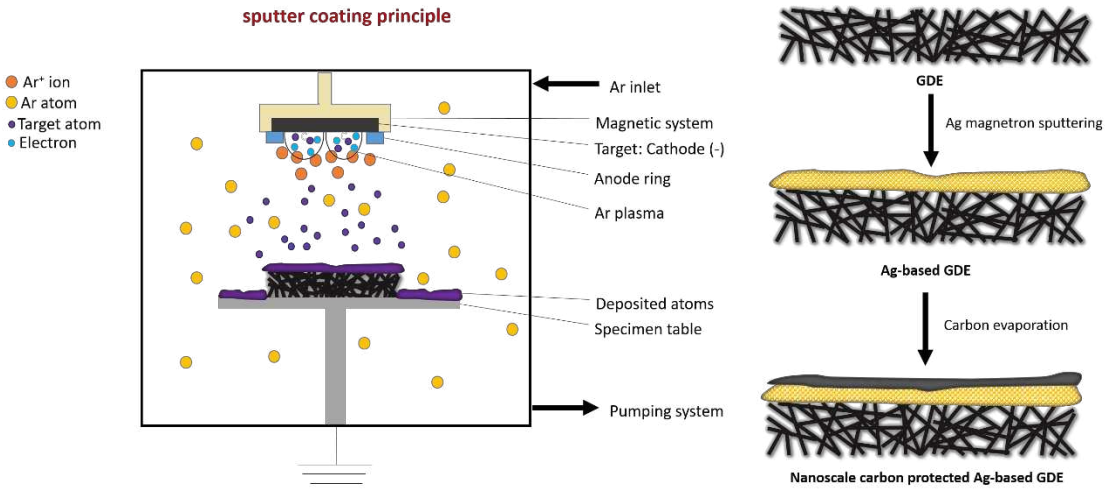

Scheme 1: Illustration of the sputter coating principle and the formation of nanoscale carbon protected Ag-based GDEs by Ag magnetron sputtering and carbon evaporation.

The samples were neither cooled nor heated during the depositions, while the sample stage continuously rotated during the sputtering/evaporation and the target-to-substrate distance was maintained at 50 mm.

2.3 Electrochemical set-up

Electrochemical measurements were performed with a multi Autolab M204. Chronopotentiometric (CP) measurements of one hour were conducted using an in-house made hybrid flow cell where the anolyte performs in batch and the catholyte is recirculated through a gas-liquid divider (a more detailed configuration can be found in Figure S2 and S4). Both compartments were separated by a Selemion® DSVN anion exchange membrane. This membrane was chosen to allow hydroxyl ions (formed at the cathode) to migrate to the anode and avoid CO_2 consumption. CO_2 was fed into the gas channel at the cathode in a flow-by configuration at 7.5 sccm, controlled by a mass flow controller (GF-080, Brooks

Instruments) The catholyte was recirculated at a flow rate of 0.2 mL min^{-1}. The back pressure was measured by a Gefran TK-series pressure sensor and logged by a I/O device (National instruments, NI6000), which was automatically read out with MATLAB® R2016a. The reacted gas stream was fed to an in-line thermo trace 1300 gas chromatograph (GC), equipped with a Thermal conductivity detector (TCD) detector and a micropacked column (ShinCarbon ST 100/120, 2 m, 1 mm ID, Restek). Finally, the gas stream was fed to a mass flow indicator to record the outlet flow, which was used for FE calculations. For both catholyte and anolyte, 1 M of $KHCO_3$ was used as the electrolyte.

A carbon cloth served as counter electrode (CE) and a leak-free Ag/AgCl electrode (W3-690053, Harvard Apparatus) was used as a reference electrode (RE) to control the applied current and to measure the corresponding potential in a three electrode set-up where the Ag-based GDE functioned as a working electrode (WE). During all measurements, the ohmic resistance in the set-ups remained between 6 and 8 ohms, evidencing that the additional carbon layer does not significantly alter the resistance of the cell. The uncompensated resistance (iR-drop) was measured at the end of the experiment by the current interrupt method (CI) which applies a lower current and measures the corresponding potential. The potential difference between the CP experiment and the iR-drop measurement was divided by the current difference of the two, which corresponds to the uncompensated resistance as expressed below.

$$iR = \frac{E_{CP,exp} - E_{CI}}{i_{CP,exp} - i_{CI}}$$

Where iR is the uncompensated resistance, $E_{CP,exp}$ and E_{CI} are the potentials from the CP experiment and the current interrupt, respectively. $i_{CP,exp}$ and i_{CI} are the currents applied during the CP and current interrupt experiment, respectively.

All potentials are reported versus the reversible hydrogen electrode (RHE), unless stated

otherwise. The potentials versus the leak-free Ag/AgCl were converted using following equation.

$$E_{RHE} = E_{ref} + 0.059\,pH + E^{\circ}_{Ag\,/\,AgCl} + iR$$

Where E_{RHE} and E_{ref} are the potentials versus the RHE and reference electrode, respectively. $E^{\circ}_{Ag/AgCl}$ is the standard electrode potential of the Ag/AgCl system. iR is the extra potential caused by the ohmic resistance.

The accessibility of water at the Ag surface was investigated using cyclic voltammetry (CV). The Ag70C15 sample was submersed in a 0.5 M KOH solution and analyzed within a potential range of -0.5 V and 0.7 V at a scan rate 50 mV s^{-1}. The reduction and oxidation peaks of Ag were investigated.

2.4 Electrode surface analysis

Contact angle measurements were performed with a Krüss GmbH DSA 10-mk2 device by drop-casting 2 µL of Milli-Q at a rate of 24.79 µL min^{-1} with a syringe plunger on the electrode surface at room temperature. The angle between the catalyst surface and the water droplet was measured by a drop-shape analysis software, repeated for several times and thereafter the average of these measurements was calculated.

The sample was further investigated from 2 different morphological perspectives. First, the surface was analyzed with a scanning electron microscope (SEM, FEI Quanta 250) at 20 kV using secondary electrons. Subsequently, cross-sections were taken from the Ag-based GDE electrodes using a focused ion beam dual beam microscope (FIB, ThermoFischer Scientifc Helios Nanolab 650). Primarily, a Pt protective layer was deposited (by ion beam induced platinum deposition at 30 kV with 0.23 nA) onto the different Ag-based GDEs in order to prevent any FIB induced damage. Thereafter, three subsequent thinning steps were performed at 30 kV, 8 kV and 2 kV, respectively, to obtain a FIB lamella. High-angle annular dark-field

scanning transmission electron microscopy (HAADF STEM) and electron energy loss spectroscopy (EELS) measurements were performed using an aberration-corrected cubed ThermoFischer Scientifc Titan electron microscope, operated at 300 kV.

Next, Raman spectra were recorded in air at room temperature using a Micro-Raman Horiba (Xplora Plus Microscope) equipped with a green 532 nm laser, in the range of 100 cm^{-1} to 3000 cm^{-1} Raman shift. This technique was used to indicate the presence of an amorphous carbon layer and investigate the evolution of the carbon layer thickness. All samples were sputtered on a glass substrate to eliminate the contribution of the GDE (carbon based).

Finally, XPS measurements were performed using a PHI - VersaProbe III using an Al X-ray source (1486.6eV) and an automatic electron neutralizer. The samples were analyzed across an area of 100 µm in diameter. High resolution scans were recorded with a pass energy of 26eV and a step size of 0.05eV. Due to the low penetration depth of XPS, Ag70 and Ag70C5 were the only two samples investigated, as thicker carbon layers would block the Ag signal.

2.5 Stability measurements

Electrochemical durability measurements were conducted using an in-house made flow set-up, allowing to operate in a three-electrode configuration (a schematic overview is presented in the Figure S3 and S4). A CO_2 flow of 25 sccm, controlled by a Brooks Instrument GF-40/100 mL min^{-1} mass flow controller, entered the cell in flow-by mode at the cathode side. Both the catholyte and anolyte flows were set to 2.6 mL min^{-1}, containing respectively 0.5 M aqueous $KHCO_3$ and 2 M aqueous KOH solutions, with a total volume of 300 mL catholyte and 500 mL anolyte, which were recycled during the experiment. A 1 cm^2 Ag-based GDE functioned as the WE, while the cathodic current was controlled by a leak-free Ag/AgCl reference electrode (Innovative Instruments, Inc.) with a multichannel Autolab potentiostat M204. A Nafion® 117 cation exchange membrane was used to separate the cathode from the anode. Since a KOH solution was used as anolyte for the stability measurements (as opposed

to the one hour CP measurements where $KHCO_3$ was used on both sides), a cation exchange membrane was preferred as otherwise hydroxyl ions would transport to the cathode and react with gaseous CO_2. The alkaline anolyte was preferred because of its benefits towards the oxygen evolution reaction (counter reaction). The reacted CO_2 stream traveled through the catholyte buffer container, which served as a gas-liquid divider (G/L divider) to prevent liquid from entering the GC, an in-line Shimadzu 2014 series GC equipped with a TCD detector and a micropacked column (Restek Shincarbon ST, 2 m length, 1 mm internal diameter, 100/120 mesh). The reacted CO_2 stream was sampled into the GC every 20 minutes throughout the entire experiment.

The results of the electrolysis were presented as Faradaic efficiencies (FE), using the formula below.

$$FE_i = \frac{n_i z_i F}{Q}$$

Where n_i is the amount of moles produced of a certain product i, z_i is the number of electrons necessary to generate one mole of product i, F is the Faradaic constant 96 485 C mol^{-1} and Q the amount of charge transferred.

3 RESULTS AND DISCUSSION

3.1 Physical properties of the catalyst

To perform efficient and selective electrocatalytic CO_2 reduction tests, a 70 nm Ag layer was deposited onto a GDE (Ag70) by magnetron sputter coating, using ionized Ar. SEM images showing the planar view of the sample are depicted in Figure 1 A-C. The Ag sputtered layer showed a rather uniform appearance with an interconnected micro-pore structure [23–25] (indicated by the red circles in Figure 1 C), even on a large scale.

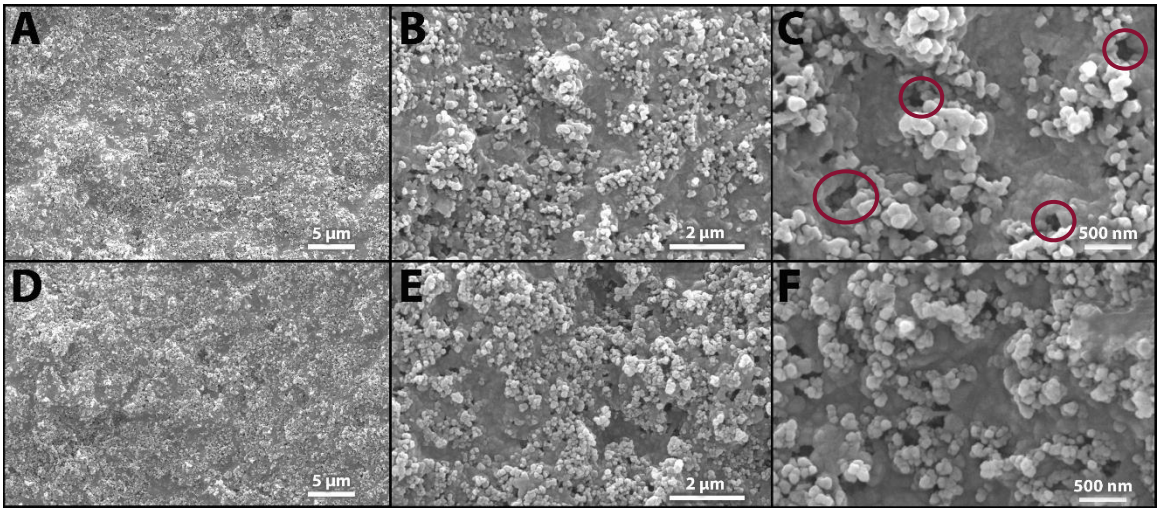

Figure 1: SEM images of a sputtered Ag-based GDE with a thickness of 70 nm at (A) 5k; (B) 20k and (C) 50k magnification and with a 15 nm thick carbon layer at (D) 5k; (E) 20k and (F) 50k magnification

A nanoscale carbon layer was deposited through carbon evaporation. Layer thicknesses of 5, 15, 20 and 30 nm (Ag70C5, Ag70C15, Ag70C20 and Ag70C30, respectively) on top of the Ag sputtered layer were obtained. Using the SEM for a top-down comparison between the Ag70 sample (Figure 1 A-C) and the Ag70C15 (Figure 1 D-F) did not show clear differences before and after the application of the carbon layer. As a result, the microporous Ag architecture remained visible even after applying the carbon coating. SEM energy dispersive X-ray spectroscopy (SEM EDS) data (Table S1) of the resulting structures however clearly indicated a difference between Ag70 and Ag70C15 in terms of the Ag/C ratio. The latter resulted in a ratio of 0.027 in contrast to the Ag70 sample where a ratio of 0.045 was obtained. This is a clear indication of a carbon layer being present at the surface of Ag70C15. In conclusion, the planar view of AG70 and Ag70C15 indicated that the addition of a carbon layer did not affect the structure of the Ag coating itself.

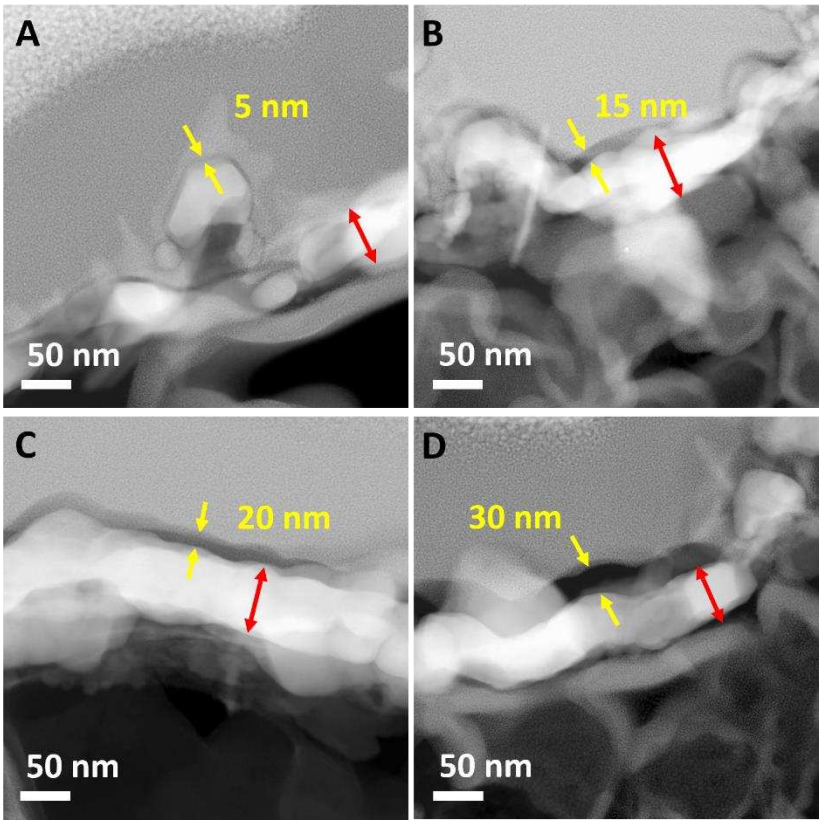

Figure 2: Cross-sectional HAADF STEM images of sample (A) Ag70C5,(B) Ag70C15, (C) Ag70C20 and (D) Ag70C30, indicating the Ag layer with the red arrow and the increased thickness of the carbon layer in each sample with yellow arrows

To further confirm the presence of the carbon layer, a cross-section of each sample was analyzed after FIB milling (Figure 2 and Figure S5). Although the electrode surface appears to be quite rough, an homogeneous Ag layer of ~70 nm is clearly observed in each sample, as well as a carbon layer with increased thickness of 5, 15, 20 and 30 nm for the Ag70C5, Ag70C15, Ag70C20 and Ag70C30 samples respectively. Importantly, for the thinner layers an inhomogeneous distribution of the carbon layer over the rough Ag surface was observed. Underneath the Ag layer, the porous GDE (carbon paper) was visible in the HAADF STEM cross-sectional images.

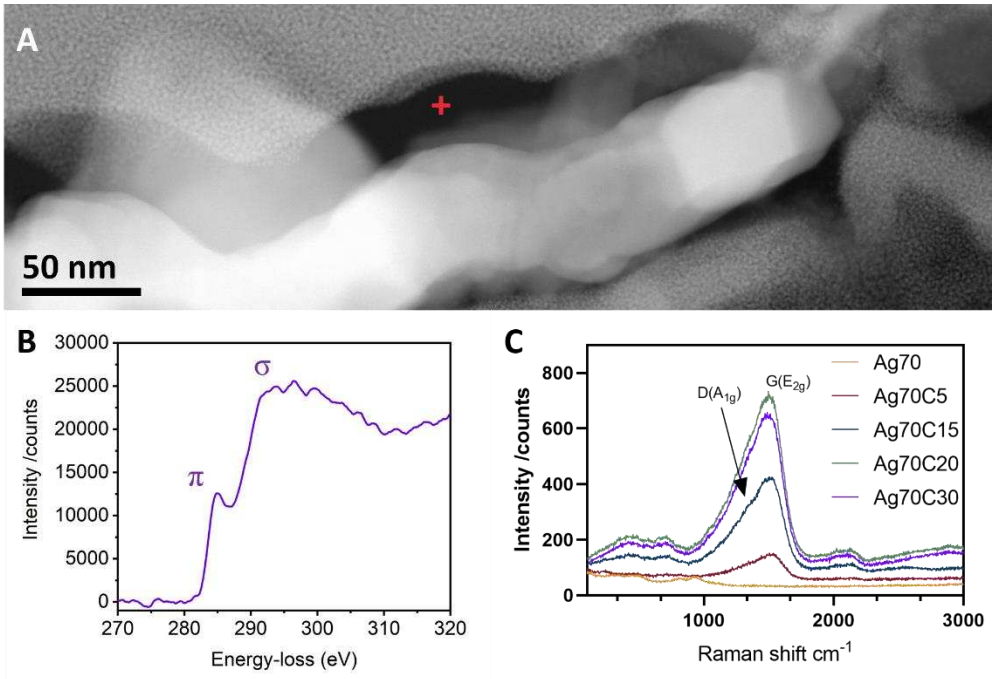

Figure 3: (A) High resolution HAADF STEM image of the carbon layer from the Ag70C30 sample and (B) EELS spectrum obtained from the red cross point indicated in the image on A, where the π and σ contribution of the C–K edge for sp^2 amorphous carbons can be observed. (C) Raman spectrum of Ag70Cx before electrochemical CO_2 reduction giving insight on the graphitization degree of the carbon layers

To investigate the graphitization degree of the carbon layers, EELS measurements were performed on sample Ag70C30 (Figure 3 A). As it has the thickest carbon layer, it is easier to obtain a reliable measurement of the carbon layer without other possible contributions from the background. The obtained EELS spectrum is shown in Figure 3 B where the characteristic shape of a sp^2-rich amorphous carbon can be observed [26]. The well-defined π peak indicate the presence of sp^2 C, while the broad σ peak indicates a lower level of crystallinity. From these results it can be concluded that the carbon layers are composed of disordered graphene-like carbon, which are well known for their high degree of porosity [27,28]. This high porosity is preferred, as it allows H^+ carriers to travel to the Ag catalyst layer.

Figure 3 C illustrates the Raman spectrum of the as-deposited carbon layer onto the Ag-based GDE electrode before the electrochemical CO_2 reduction. As shown in the graph, one main peak appears at 1568 cm^{-1} and one shoulder at 1361 cm^{-1}, which correspond to the G (E_{2g}) and D (A_{1g}) bands, respectively [29–32] and are visible in all carbon samples. The D maximum

originates from the movement of neighboring atoms in radial directions in the plane and is caused by structural defects, often called the disorder-induced mode. The G maximum corresponds to the movements of atoms in opposite directions perpendicular to the plane and causes C-C bond stretching [33,34]. These two bands are typical features present in amorphous carbon materials and combined with the absence of the 2D band (at about 2700 cm^{-1}, characteristic to bulk or multilayer graphite/graphene-related materials) [30,35], clearly indicate that a nanoscale amorphous carbon surface layer is present at the Ag-based GDE electrode. In addition, upon increasing the carbon layer thickness, the intensity of the carbon related maxima increased, an observation which confirms the trend already proven by the HAADF STEM experiments. It however appears that at a certain point saturation of the signal occurs as the maxima of Ag70C20 and Ag70C30 were similar. From this spectrum it can also be noted that metallic Ag is Raman insensitive as it is not polarizable during the molecular vibration. The signal that was visible during the measurements originated from the glass substrate.

To further confirm this, a CV measurement of Ag70C15 in 0.5 M KOH was performed based on the suggestion of the reviewer to investigate the porosity of the carbon layer. The oxidation and reduction of Ag manifests itself in Figure S 6. This demonstrates that the Ag catalyst layer is accessible for an electrochemical reaction.

In order to investigate the nature of the Ag catalyst layer and the influence of the carbon layer on Ag, XPS measurements were performed. Figure 4 show the XPS spectra of Ag3d and C1s, respectively. Two asymmetric Ag peaks, separated by 6 eV, at 368.5 eV ($Ag3d_{5/2}$) and 374.5 eV ($Ag3d_{3/2}$) could be observed. This indicates that Ag0 is predominantly present in the sample of each spin-orbit component for Ag metal. These peaks were both accompanied by low loss features to their higher binding energy side. Comparing both samples, the Ag signal was more pronounced for the Ag70 sample, whereas the carbon signal was increased in the

Ag70C5 sample.

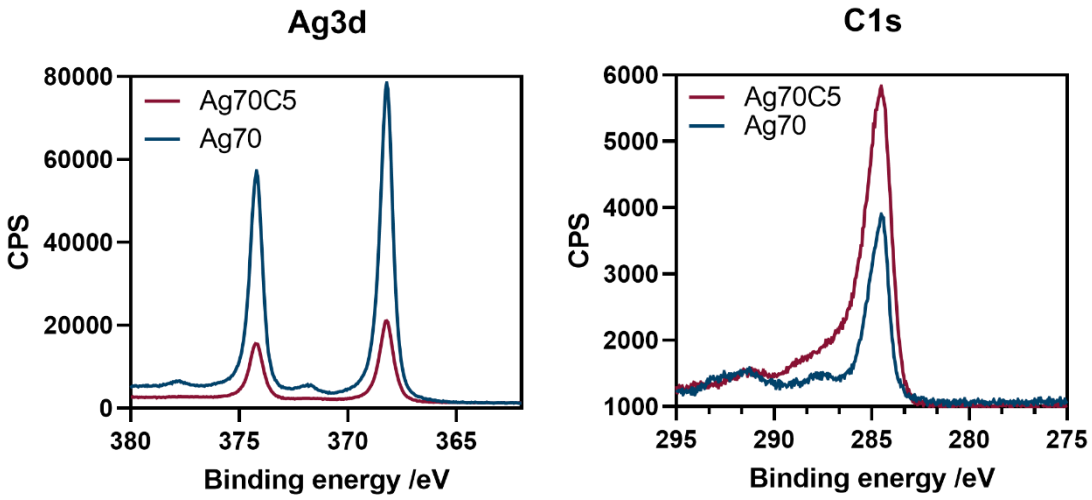

Figure 4: High resolution spectra of Ag3d and C1s. Ag70C5 is represented in red and Ag70 in blue

Nevertheless, no clear difference between the two samples can be observed (Figure S 7), which most likely means that Ag and C do not bind directly to each other. This is further confirmed by the absence of additional peaks at lower binding energies in the Ag3d spectrum, as they typically occur in literature reports where Ag-C bonds are formed.[36] These findings thus support our hypothesis that the Ag catalyst is not chemically bonded to the carbon layer and that the carbon layer will not interfere with the selectivity of the Ag layer towards eCO_2R but rather solely serves as a protective layer.

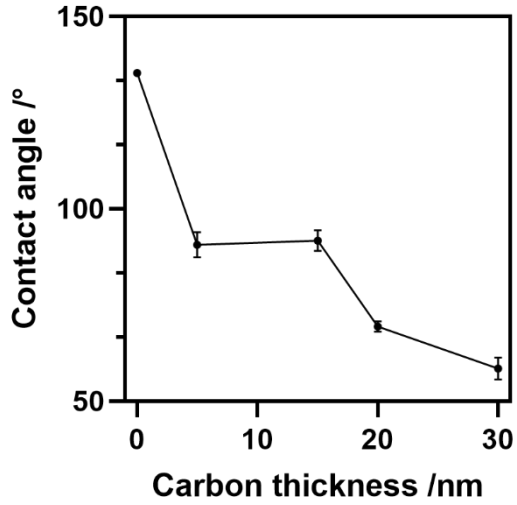

Figure 5: Contact angles as a function of the amorphous carbon layer thickness on Ag-based GDEs prior to CO_2 reduction experiments with layer thicknesses reaching from 0 nm to 30 nm

Contact angles of Ag70, Ag70C5, Ag70C15, Ag70C20 and Ag70C30 were measured prior to the electrochemical CO_2 reduction reaction. A contact angle of 135.3° was measured at Ag70, where a carbon coating was absent. This angle decreased upon addition of a 5 nm carbon layer to 90.6° and declined to 58.5° at 30 nm of carbon coating, as shown in Figure 5 (images of the corresponding contact angles are depicted in Figure S8). The difference in wettability between Ag70 and the Ag70Cx can be due to the varying roughness of the surface [37–40]. When the surface roughness increases, the contact angle increases as well, as was reported by Wenzel on non-wettable surfaces [41]. The GDE substrate is known to be a rough surface and by depositing the Ag layer by sputtering, this layer also expressed a certain roughness. Upon addition of a carbon layer, the roughness however decreased, which might seem a contradiction but can be explained as follows. The carbon layer was applied by evaporation, which is a different method compared to the Ag layer deposition (which was deposited by sputtering). This type of method is typically used to obtain better 'step coverage' with a smoother surface as a result. At first the carbon layer is very thin (only 5 nm thick), but increasing the layer thickness, created a better step coverage, leading to an even smoother surface yielding lower contact angles [42,43].

3.2 Nanoscale carbon layers and their effect on the performance of Ag-based GDEs

Electrochemical experiments were executed in a hybrid flow reactor as depicted in Figure S2 and S4. The FEs of compounds in the gas phase were recorded during a period of 1 hour with intermediate sampling every 15 min, starting at 5 min after applying a current of 100 mA cm^{-2}. The evolution of the FE over time of the Ag-based GDEs with altering carbon layer thickness are shown in Figure 6.

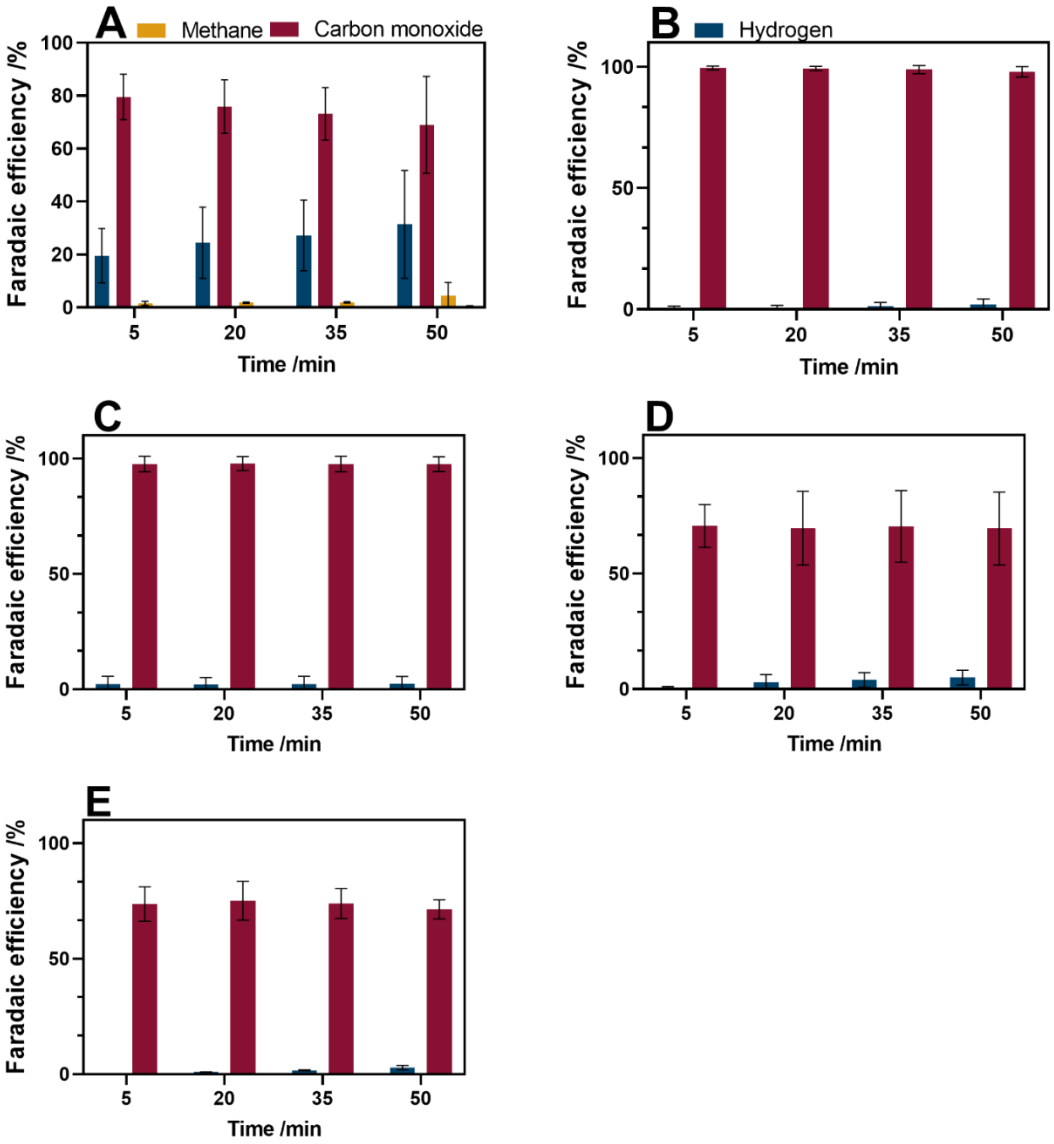

Figure 6: Evolution in FE of H_2 (blue); CO (red) and CH_4 (orange) during an 1 h electrolysis experiment for samples (A) Ag70; (B) Ag70C5; (C) Ag70C15; (D) Ag70C20 and (E) Ag70C30

Considering the electrolysis experiment of Ag70, a pronounced amount of H_2 was already formed at the beginning of the measurement. The H_2 increased over time from 19.6 % at the beginning to 31.4 % after 50 min of running time. The gradual increase in H_2 production impacted the CO formation with a consequent reduction in its FE over time. Initially, the FE of CO reached up to 79.5 % which waned to 69.0 %. Additionally, methane was also detected as a reaction product and along with the H_2 experienced an increase in FE up to 4.5 % after 50 min of electrolysis. We hypothesize that this development in methane production is related to the migration of Cu to the surface during electrolysis, which was already reported in literature on CuAg bimetallic surfaces [44]. Ethylene was also present in the reacted flow, but only in very low amounts resulting in a FE of 0.3 % (not represented in the graph). The production of methane and ethylene can be attributed to the trace amount of Cu (originating from the sputter equipment) present inside the Ag layer, as shown in Figure S9.

Compared to the literature of Ag-based GDEs [45–49], the FE of CO was rather low and a considerable amount of H_2 was produced at the end of the experiment. This can be attributed to the intensive flooding occurring throughout the experiment, as a consequence of the lower Ag loading present on the substrate compared to literature. Flooding is a well-known problem within this field of research. Literature states that this is due to electro-wetting [50,51], which is a possible cause for the increasing amount of H_2 produced during the electrolysis. It is known that the passage of faradaic current accelerates flooding and is consistently reported in literature [50,52]. Increasing the current density seemed to be beneficial for the appearance of flooding, which initiates carbonate precipitation and eventually can lead to GDE failure [50].

In order to inhibit the production of hydrogen, an amorphous carbon layer was deposited onto the existing Ag-based GDEs with altering layer thicknesses. The amorphous carbon layers in this paper differentiate themselves from other studies in terms of their simplicity and thickness. Often, the chemical nature of the catalyst surface was modified by either additives

during the catalyst synthesis [16] or by modifying the existing electrode surface [15,17,18,53,54]. These catalyst adaptions severely influenced the hydrophobicity of the surface and participate in the stabilization of the intermediates, altering the product distribution. On the contrary, here, only a nanoscale amorphous carbon layer was deposited and additional functional groups were absent, preserving the intrinsic function of the electrocatalyst. This is a cost-efficient, easy and faster way to prepare electrocatalysts with HER inhibiting properties.

As a result, as shown in Figure 6 B, only a 5 nm thick carbon layer was necessary to inhibit the HER. At the beginning of the measurement, hydrogen formation was reduced to a FE of 0.5 % leading to a FE of 99.5 % of CO. Throughout the experiment, the FE of H_2 increased slowly and eventually accounted for 2.1 %, which was accompanied by a small decrease in FE of CO to 97.9 %. The HER suppression could be attributed to the diffusion-selective carbon layer [55]. This porous carbon layer acts as a physical barrier between the catalyst layer and the electrolyte, preventing direct contact. The carbon layer drastically lowers the diffusion of proton carriers to the Ag catalyst surface. The CO_2 molecules are supplied from the backside of the GDE and can easily reach the Ag catalyst layer. Due to the limited amount of protons at the Ag interface, CO_2 reduction is promoted and the HER is suppressed [56]. In addition, liquid passing through the outlet gas channel was absent. Despite the contradiction of the decrease in contact angle, the carbon layer seems to prevent flooding. This difference in contact angle can be explained by the different deposition methods between Ag and carbon (as elucidated in 3.1). Nevertheless, since carbon is more hydrophobic than Ag, a decrease in flooding is observed. This flooding was visible with the naked eye in all experiments in the hybrid cell where the carbon layer was absent and disappeared upon deposition of a carbon layer.

Depositing a carbon layer of 15 nm resulted in a FE of 2.4 % for H_2 and 97.6 % for CO, which were thus within the same range as the previous layer thicknesses. Interestingly, the

addition of an amorphous carbon layer also lowered the cathodic working potential from -1.79 V (Ag70) to -1.63 V (Ag70C15), which is a reduction of 0.16 V. By reducing the overpotential at the cathode, the energy-efficiency increased.

Increasing the thickness even further, entailed a decrease in the FE towards CO and in addition the total FE no longer reached 100 %. Total FE's of around 69.5 % and 71.3 % were observed when depositing 20 nm and 30 nm of carbon, respectively. This discrepancy could not be accounted for by analyzing the liquid phase, as only traces of formate were observed. Since these layer thicknesses underperformed, they were not considered for further investigation. Moreover, the determination of the Faradaic losses are complex and lay beyond the scope of this work.

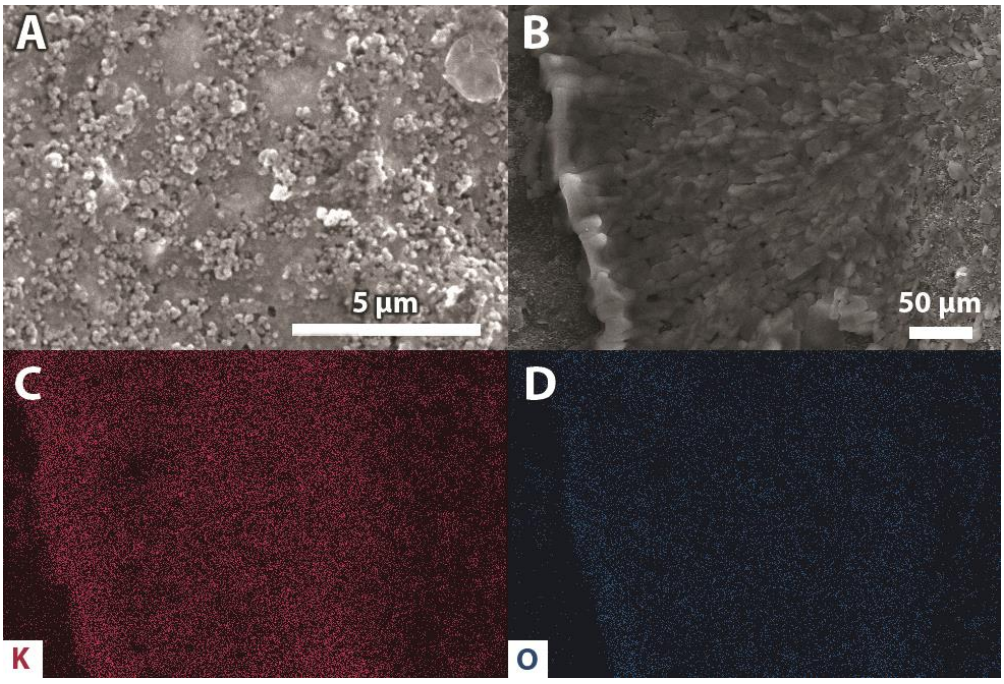

Figure 7: SEM images of AG70C20 (A) before and (B) after 1 h of electrolysis and the corresponding SEM EDS maps of (C) potassium and (D) oxygen after 1 h electrolysis

Additionally, Figure 7 A and B depict the SEM images of the Ag70C20 sample before and after the electrolysis experiment and after thoroughly rinsing the electrode with milliQ at the end of the measurement. Comparing both SEM images, it is clear that still an additional layer exists after using the Ag-based GDE in the hybrid flow cell. To confirm the presence of

$KHCO_3$ deposits, SEM EDS maps (Figure 7 C and D) were recorded. These maps indeed indicate that the additional layer consisted of potassium and oxygen, which was absent prior to the experiment. This indicates the precipitation of salt from the electrolyte onto the electrocatalyst surface.

In addition, Raman spectra were collected on the same sample to support the SEM and SEM EDS data. The Raman spectra, depicted in Figure S10, show a clear difference between the two samples which supported the SEM and SEM EDS data from Figure 7. The Ag70C20 sample before the experiment was in accordance with Ag70C15 (Figure 3 C) when comparing both Raman spectra. Nevertheless, investigating the sample after the electrolysis, a clear difference could be observed. In this case, the presence of CO_3^{2-} could be confirmed due to the characteristic peaks at 681 cm^{-1} and 1047 cm^{-1}, which were absent before electrolysis [57]. These results, in combination with the SEM EDS maps, prove the presence of an electrolyte salt layer deposited on top of the Ag70C20 sample.

In conclusion, the amorphous carbon layer seemed to be beneficial for the inhibition of the HER and CO formation, at least in terms of FE. A decrease in overpotential was ensured and the EASA was preserved, despite the deposition of an additional layer on top of the Ag catalyst layer. A carbon layer thickness beyond 15 nm resulted in a decrease in total FE, which could not be accounted for by analyzing the liquid phase. A thickness of 15 nm was selected to be most ideal to pursue further experiments because of the persistence in FE compared to the other layers.

3.3 Superior durability of carbon coated Ag-based GDEs

Ag70 and Ag70C15 were both subjected to more industrially relevant conditions over a longer period of time. The production of H_2 and CO were logged every 20 min during 6 hours.

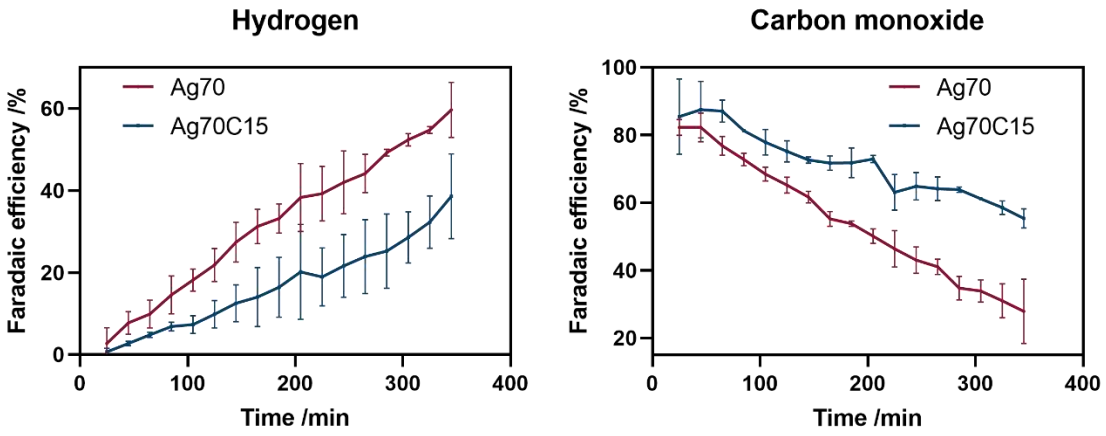

Figure 8: Inhibition of H_2 by a naoscale carbon layer on Ag-based GDEs expressed in the evolution of the faradaic efficiency of CO and H_2 during the experiment

Figure 8 depicts the evolution in H_2 and CO production over time. A distinct difference existed between Ag70 and Ag70C15. Ag70 showed a precipitous increase in H_2 production, which consequently led to a faster decrease in CO production. At Ag70C15, the HER was inhibited by the additional carbon layer on the Ag-based GDE. A difference of 21 % in FE of H_2 was present between Ag70 and Ag70C15 at the end of the 6 hours of measurement, with FE reaching 60 % and 39 % for Ag70 and Ag70C15, respectively. The FE of CO decreased to 55 % over Ag70C15 and 28 % over Ag70, which is a difference of 27 % between the two electrocatalysts. The FE of CO diminished by 54.4 % at Ag70 compared to 30.2 % at Ag70C15. Additionally, an overall increase in HER of 56.9 % was observed at Ag70, which was only 37.9 % at Ag70C15. It is clear that the amorphous carbon layer inhibits the HER production over longer periods of time. After 6 hours, an improvement of 150 % could be obtained.

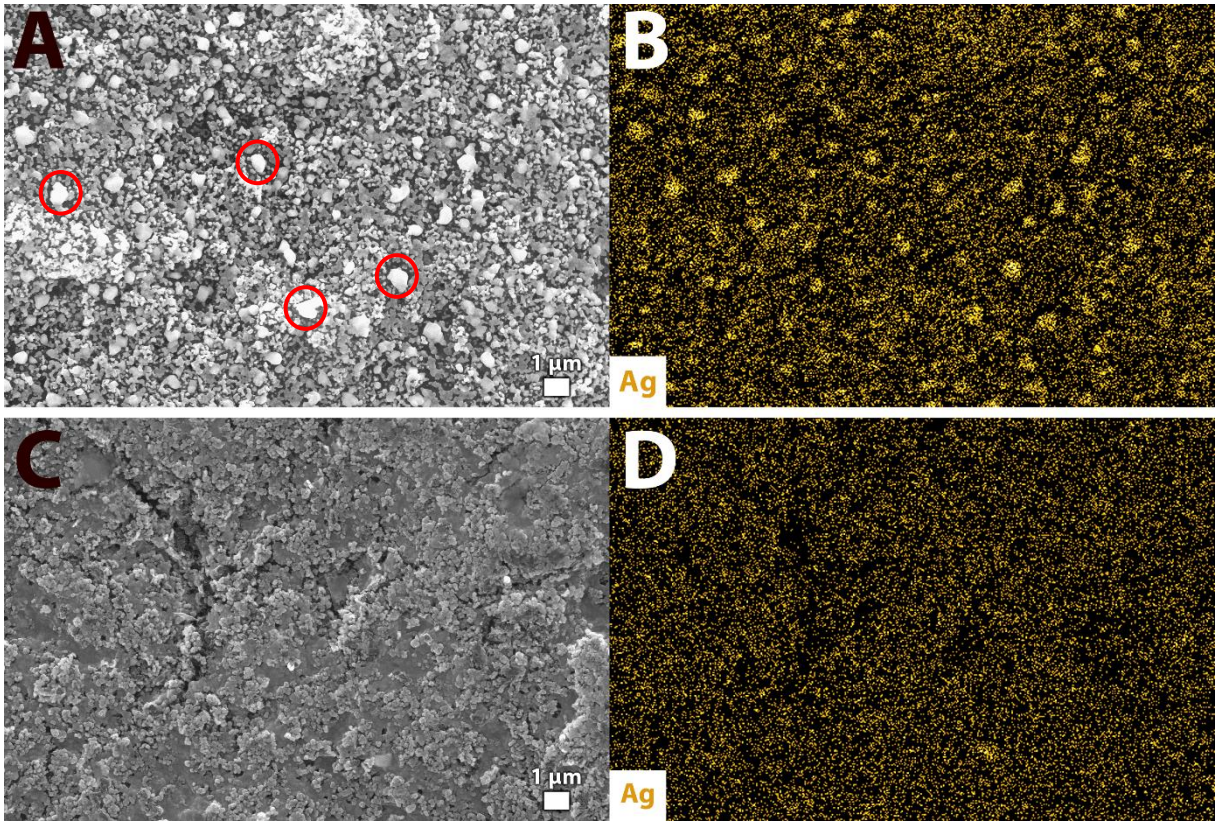

Figure 9: SEM image of (A) Ag70 after 3 hours of experiment, (C) Ag70C15 after 5 hours of experiment and (B and D) the corresponding SEM EDS maps of Ag

Comparing the surfaces of Ag70 and Ag70C15 after 3 h and 5 h of the experiment, respectively, clearly indicated a difference between the two electrodes. As depicted in Figure 9, clustering of Ag on the surface of the electrode, indicated by the red circles, was visible. This clustering is absent on the Ag70C15 surface. This proves the stabilizing effect of the amorphous carbon layer, since it inhibits the movement of the Ag particles on the surface and thereby prevents the clustering of the Ag on the surface.

4 CONCLUSION

In this study we investigated the inhibition of the HER by applying a carbon top layer on a typical CO_2 reduction catalyst as it typically lowers the overall energy efficiency of the process. At the same time, we also explored the stabilizing effect of porous low loading electrocatalysts (~70 µg cm^{-2}). As most studies use surface modifiers to alter the chemical nature of the surface and use very thick protective layers, we investigated the effect of

nanoscale amorphous carbon layers on the HER and stability, preserving the chemical nature of the electrocatalyst itself. In comparison with previously mentioned literature, this is a straightforward and fast modification that can be done after catalyst synthesis and deposition on the GDE.

In this investigation, we used Ag-based GDEs as a benchmark, which were synthesized by magnetron sputtering. Additionally, porous amorphous carbon was added by carbon evaporation. By using Ag-based GDEs, we were able to highlight the effect of carbon on the HER inhibition since they are not prone to produce products other than H_2 and CO. In addition, the porous carbon layer allows the H^+-carriers to diffuse to the Ag catalyst layer, without any excess of protons. Since the CO_2 is supplied from the backside of the GDE, it is sufficiently available at the Ag catalyst surface.

Upon applying a porous amorphous carbon layer onto the Ag-based GDEs, we noticed that the Ag catalyst is attainable, since Ag oxidation and reduction could be observed during the CV measurements. It has also been perceived during the XPS measurement that the Ag catalyst layers was not chemically bonded to the carbon layer. This carbon layer resulted in the inhibition of the HER and preventing the catholyte from traveling through the GDE.

Carbon layers thinner than 15 nm already showed to be less stable after 1 hour. Increasing the layer thickness to 20 nm or even 30 nm led to a decrease in total faradaic efficiency. Considering the above, a layer thickness of 15 nm is most ideal to perform long term experiments.

By comparing the bare Ag-based electrode, after a measurement of 6 hours, against the carbon coated Ag-based GDE, a remarkable difference in the produced amount of hydrogen, was obtained. The HER accounted for 39 % on the latter electrode in contrast to 60 % at the former electrode. This is an increase in FE of 56.9 % using the Ag70 catalyst and only 37.9

% when carbon was applied, which led to an improvement of 150 %. Additionally, the carbon layer ensured that the distribution of Ag catalyst across the electrocatalyst surface was maintained throughout the experiment. This is in contrast to the bare Ag electrode, which encountered destabilization due to sintering.

We show the great potential of using a carbon layer as HER inhibitor and stabilizing layer. This carbon layer was applied separately from the actual catalytic layer, highlighting the ease of use. This highlights the applicability of the carbon layer in electrocatalysis for several other catalysts as this could help to increase the durability of the system and as such the economic feasibility as well.

5 ASSOCIATED CONTENT

5.1 Supporting Information

Photograph of the Ag70Cx samples (Figure S1); Schematic representation of the hybrid flow reactor (Figure S2); Schematic representation of the flow reactor for durability measurements (Figure S3); Photographs of hybrid flow cell and flow reactor (Figure S4); Table of the at% of Ag and carbon in Ag-based catalysts (Table S1); Cross sectional HAADF STEM images of Ag70Cx (Figure S5); CV measurement of Ag70C15 (Figure S6); Normalized high resolution XPS spectra of Ag70 and Ag70C5 (Figure S7); Images of contact angle measurements (Figure S8); SEM EDS spectrum of the Ag70 (Figure S9) and Raman spectra of Ag70C20 before and after electrolysis (Figure S10).

6 AUTHORS INFORMATION

Corresponding Authors

Tom.Breugelmans@uantwerpen.be

7 ACKNOWLEDGEMENTS

L. Pacquets was supported through a PhD fellowship strategic basic research (1S56920N) of the Research Foundation – Flanders (FWO). S.B. acknowledges financial support from ERC

Consolidator Grant Number 815128 REALNANO. This research was financed by the research counsel of the university of Antwerp (BOF-GOA 33928). P. Cool and R.-G. Ciocarlan acknowledge financial support by FWO Flanders (project no. G038215N). The authors recognize the contribution of S. Pourbabak and T. Derez for the assistance with the Ag and carbon coating, Indah Prihatiningtyas and Bart Van der Bruggen for the assistance with the contact angle measurements, Daniel Choukroun for the use of the in-house made hybrid flow cell and Stijn Van den Broeck for his assistance with the FIB measurements.

8 REFERENCES

1. Umeda, M., Niitsuma, Y., Horikawa, T., Matsuda, S. & Osawa, M. Electrochemical Reduction of CO_2 to Methane on Platinum Catalysts without Overpotentials: Strategies for Improving Conversion Efficiency. *ACS Appl. Mater. Interfaces* (2020) doi:10.1021/acsaem.9b02178.
2. Andreoli, E. CO_2-to-ethylene electroreduction gets a boost. *Nat. Catal.* 8–9 (2021).
3. Sun, K., Wu, L., Qin, W., Zhou, J., Hu, Y., Jiang, Z., Shen, B. & Wang, Z. Enhanced electrochemical reduction of CO_2 to CO on Ag electrocatalysts with increased unoccupied density of states. *J. Mater. Chem. A* **4**, 12616–12623 (2016).
4. Fan, L., Xia, C., Zhu, P., Lu, Y. & Wang, H. Electrochemical CO_2 reduction to high-concentration pure formic acid solutions in an all-solid-state reactor. *Nat. Commun.* **11**, 1–9 (2020).
5. Whipple, D. T. & Kenis, P. J. A. Prospects of CO_2 Utilization via Direct Heterogeneous Electrochemical Reduction Devin. *J. Phys. Chem. Lett.* 3451–3458 (2010).
6. Lee, H., Yang, K. D., Yoon, S. M., Ahn, H., Lee, Y. Y., Chang, H. Jeong, D. H., Lee, Y., Kim, M. Y. & Nam, K. T. Concave Rhombic Dodecahedral Au Nanocatalyst with Multiple High-Index Facets for CO_2 Reduction. *ACS Nano* 8384–8393 (2015).
7. Valenti, M., Valenti, M., Prasad, N. P., Kas, R., Bohra, D., Ma, M., Balasubramanian, V., Chu, L., Gimenez, S., Bisquert, J., Dam, B. & Smith, W. A. Suppressing H_2 Evolution and Promoting Selective CO_2 Electroreduction to CO at Low Overpotentials by Alloying Au with Pd. *ACS Catal.* **9**, 3527–3536 (2019).
8. He, J., Johnson, N. J. J., Huang, A. & Berlinguette, C. P. Electrocatalytic Alloys for CO_2 Reduction. *ChemSusChem* 48–57 (2018) doi:10.1002/cssc.201701825.
9. Lee, J. H., Kattel, S., Jiang, Z., Xie, Z., Yao, S., Tackett, B. M., Xu, W., Marinkovic, N. S. & Chen, J. G. Tuning the activity and selectivity of electroreduction of CO_2 to synthesis gas using bimetallic catalysts. *Nat. Commun.* **10**, 1–8 (2019).
10. Wang, J., Zheng, X., Wang, G., Cao, Y., Ding, W., Zhang, J., Wu, H., Ding, J., Hu, H., Han, X., Ma, T., Deng, Y. & Hu, W. Defective Bimetallic Selenides for Selective CO_2 Electroreduction to CO. *Adv. Mater.* **34**, 1–8 (2022).
11. Wang, J. J., Li, X. P., Cui, B. F., Zhang, Z., Hu, X. F., Ding, J., Deng, Y. D., Han, X. P. & Hu, W. B. A review of non-noble metal-based electrocatalysts for CO_2 electroreduction. *Rare Met.* **40**, 3019–3037 (2021).

12. Marcandalli, G., Goyal, A. & Koper, M. T. M. Electrolyte Effects on the Faradaic Efficiency of CO_2 Reduction to CO on a Gold Electrode. *ACS Catal.* (2021) doi:10.1021/acscatal.1c00272.

13. Kim, B., Ma, S., Jhong, H. M. & Kenis, P. J. A. Influence of dilute feed and pH on electrochemical reduction of CO_2 to CO on Ag in a continuous flow electrolyzer. **166**, 271–276 (2015).

14. Vennekoetter, J., Sengpiel, R. & Wessling, M. Beyond the catalyst : How electrode and reactor design determine the product spectrum during electrochemical CO_2 reduction. *Chem. Eng. J.* **364**, 89–101 (2019).

15. Buckley, A. K., Lee, M., Cheng, T., Kazantsev, R. V., Larson, D. M., Goddard, W. A., Toste, F. D. & Toma, F. M. Electrocatalysis at organic-metal interfaces: Identification of structure-reactivity relationships for CO_2 reduction at modified cu surfaces. *J. Am. Chem. Soc.* **141**, 7355–7364 (2019).

16. Ahn, S., Klyukin, K., Wakeham, R. J., Rudd, J. A., Lewis, A. R., Alexander, S., Carla, F., Alexandrov, V. & Andreoli, E. Poly-Amide Modified Copper Foam Electrodes for Enhanced Electrochemical Reduction of Carbon Dioxide. *ACS Catal.* **8**, 4132–4142 (2018).

17. Kim, C., Eom, T., Jee, M; S., Jung, H., Kim, H., Min, B. K. & Hwang, Y. J. Insight into Electrochemical CO_2 Reduction on Surface-Molecule-Mediated Ag Nanoparticles. *ACS Catal.* **7**, 779–785 (2017).

18. Sakamoto, N. & Arai, T. Enhanced electrochemical CO_2 reduction selectivity by application of self-assembled polymer microparticles to a silver electrode. *Chem. Commun.* **55**, 11623–11625 (2019).

19. Yue, P., Fu, Q., Li, J., Zhang, L., Xing, L., Kang, Z. & Liao, Q. Triple-phase electrocatalysis for the enhanced CO_2 reduction to HCOOH on a hydrophobic surface. *Chem. Eng. J.* **405**, 126975 (2021).

20. Hsieh, Y., Betancourt, L. E., Senanayake, S. D., Hu, E., Zhang, Y., Xu, W. & Polyansky, D. E. Modification of CO_2 reduction activity of nanostructured silver electrocatalysts by surface halide anions. *ACS Appl. Energy Mater.* **2**, 102–109 (2019).

21. Han, X. & Thoi, V. S. Non-Innocent Role of Porous Carbon Towards Enhancing C_{2-3} Products in Electroreduction of Carbon Dioxide. *ACS Appl. Mater. Interfaces* (2020) doi:10.1021/acsami.0c10591.

22. Dinh, C., Burdyny, T., Kibria, G., Seifitokaldani, A., Gabardo, C. M., Arquer, F. P. G. D., Kiani, A., Edwards, J. P., Luna, P. D., Bushuyev, O. S., Zou, C., Quintero-bermudez, R., Pang, Y., Sinton, D. & Sargent, E. H. CO_2 electroreduction to ethylene via hydroxide-mediated copper catalysis at an abrupt interface. *Electrochemistry* **787**, 783–787 (2018).

23. Kelly, P. J., O'Brien, J. & Arnell, R. D. The production of porous and chemically reactive coatings by magnetron sputtering. *Vacuum* **74**, 1–10 (2004).

24. Alvarez, R., García-Martín, J. M., MacÍas-Montero, M., Gonzalez-Garcia, L., González, J. C., Rico, V., Perlich, J., Cotrino, J., González-Elipe, A. R. & Palmero, A. Growth regimes of porous gold thin films deposited by magnetron sputtering at oblique incidence: From compact to columnar microstructures. *Nanotechnology* **24**, (2013).

25. Dedoncker, R., Rijckaert, H. & Depla, D. Sputter deposition of porous thin films from metal/NaCl powder targets. *Appl. Phys. Lett.* **115**, (2019).

26. Bernier, N., Bocquet, F., Allouche, A., Saikaly, W., Brosset, C., Thibault, J. & Charaï, A. A methodology to optimize the quantification of sp2 carbon fraction from K edge EELS spectra. *J. Electron Spectros. Relat. Phenomena* **164**, 34–43 (2008).

27. Wang, Y., Zhu, Y. & Wu, H. Porous characteristics of three-dimensional disordered graphene networks. *Crystals* **11**, (2021).

28. Martin, J. W., De Tomas, C., Suarez-Martinez, I., Kraft, M. & Marks, N. A. Topology of disordered 3D graphene networks. *Phys. Rev. Lett.* **123**, 116105 (2019).

29. Jin, X., He, R. & Dai, S. Electrochemical Graphitization: An Efficient Conversion of Amorphous Carbons to Nanostructured Graphites. *Chem. - A Eur. J.* **23**, 11455–11459 (2017).

30. An, B. S., Kwon, Y., Oh, J. S., Lee, C., Choi, S., Kim, H., Lee, M., Pae, S. & Yang, C. W. Characteristics of an Amorphous Carbon Layer as a Diffusion Barrier for an Advanced Copper Interconnect. *ACS Appl. Mater. Interfaces* **12**, 3104–3113 (2020).

31. Kesavan, A. V., Lee, B. R., Son, K. R., Khot, A. C., Dongale, T. D., Murugadoss, V., Ramamurthy, P. C. & Kim, T. G. Work Function-Tunable Amorphous Carbon-Silver Nanocomposite Hybrid Electrode for Optoelectronic Applications. *ACS Appl. Mater. Interfaces* **13**, 4284–4293 (2021).

32. Daems, N., Sheng, X., Vankelecom, I. F. J. & Pescarmona, P. P. Metal-free doped carbon materials as electrocatalysts for the oxygen reduction reaction. *J. Mater. Chem. A* **2**, 4085–4110 (2014).

33. Dychalska, A., Popielarski, P., Franków, W., Fabisiak, K., Paprocki, K. & Szybowicz, M. Study of CVD diamond layers with amorphous carbon admixture by Raman scattering spectroscopy. *Mater. Sci. Pol.* **33**, 799–805 (2015).

34. Gupta, S. & Narayan, J. Reduced Graphene Oxide/Amorphous Carbon P-N Junctions: Nanosecond Laser Patterning. *ACS Appl. Mater. Interfaces* **11**, 24318–24330 (2019).

35. Childres, I., L.A., J., Park, W., Cao, H. & Chen, J. P. Raman spectroscopy of graphene and related materials. *New Dev. Phot. Mater. Res.* (2013).

36. Boukhvalov, D. W., Zhidkov, I. S., Kurmaev, E. Z., Fazio, E., Cholakh, S. O. & D'Urso, L. Atomic and electronic structures of stable linear carbon chains on Ag-nanoparticles. *Carbon N. Y.* **128**, 296–301 (2018).

37. Hideo Nakae, Ryuichi Inui, Yosuke Hirata & Hiroyuki Saito. Effects of surface roughness on wettability. *Acta Mater.* **46**, 2313–2318 (1998).

38. Kubiak, K. J., Wilson, M. C. T., Mathia, T. G. & Carval, P. Wettability versus roughness of engineering surfaces. *Wear* **271**, 523–528 (2011).

39. Xiong, B., Li, J., He, C., Tang, X., Lv, Z., Li, X. & Yan, X. Effect of pore morphology and surface roughness on wettability of porous titania films. *Mater. Res. Express* **7**, (2020).

40. Gu, H., Wang, C., Gong, S., Mei, Y., Li, H. & Ma, W. Investigation on contact angle measurement methods and wettability transition of porous surfaces. *Surf. Coatings Technol.* **292**, 72–77 (2016).

41. Cassie, A. B. D. & Baxter, S. Wettability of Porous Surfaces. *Trans. Faraday Soc.* **40**, 546–551 (1944).

42. Han, W. K., Hwang, G. H., Hong, S. J., An, H. H., Yoon, C. S., Kim, J. H., Lee, M. J., Hong, G., Park, K. S. & Kang, S. G. Complete filling of 41 nm trench pattern using Cu seed layer deposited by SAM-modified electroless plating and electron-beam evaporation. *Appl. Surf. Sci.* **256**, 2649–2653 (2010).

43. Marmur, A., Volpe, C. Della, Siboni, S., Amirfazli, A. & Drelich, J. W. Contact angles and wettability: Towards common and accurate terminology. *Surf. Innov.* **5**, 3–8 (2017).

44. Wilde, P., O'Mara, P. B., Junqueira, J. R.C., Tarnev, T., Benedetti, T. M., Andronescu, C.,

Chen, Y. T., Tilley, R. D., Schuhmann, W. & Gooding, J. J. Is Cu instability during the CO_2 reduction reaction governed by the applied potential or the local CO concentration? *Chem. Sci.* **12**, 4028–4033 (2021).

45. Verma, S., Lu, X., Ma, S., Masel, R. I. & Kenis, P. J. A. The effect of electrolyte composition on the electroreduction of CO_2 to CO on Ag based gas diffusion electrodes. *Phys. Chem. Chem. Phys.* **18**, 7075–7084 (2016).

46. Dinh, C. T., García De Arquer, F. P., Sinton, D. & Sargent, E. H. High rate, selective, and stable electroreduction of CO_2 to CO in basic and neutral media. *ACS Energy Lett.* **3**, 2835–2840 (2018).

47. Wang, R., Haspel, H., Pustovarenko, A., Dikhtiarenko, A., Russkikh, A., Shterk, G., Osadchii, D., Ould-chikh, S., Ma, M., Smith, W. A., Takanabe, K., Kapteijn, F. & Gascon, J. Maximizing Ag Utilization in High-Rate CO_2 Electrochemical Reduction with a Coordination Polymer-Mediated Gas Diffusion Electrode. *ACS Energy Lett.* **4**, 2024–2031 (2019).

48. Ma, S., Luo, R., Gold, J. I., Yu, A. Z., Kim, B. & Kenis, P. J.A. Carbon nanotube containing Ag catalyst layers for efficient and selective reduction of carbon dioxide. *J. Mater. Chem. A* (2016) doi:10.1039/C6TA00427J.

49. Endrodi, B., Bencsik, C., Darvas, F., Jones, R., Rajeshwar, K. & Janaky, C. Continuous-flow electroreduction of carbon dioxide. *Prog. Energy Combust. Sci.* **62**, 133–154 (2017).

50. Leonard, M. E., Clarke, L. E., Forner-Cuenca, A., Brown, S. M. & Brushett, F. R. Investigating Electrode Flooding in a Flowing Electrolyte, Gas-Fed Carbon Dioxide Electrolyzer. *ChemSusChem* **13**, 400–411 (2020).

51. Burchardt, T. An evaluation of electrocatalytic activity and stability for air electrodes. *J. Power Sources* **135**, 192–197 (2004).

52. Verma, S., Hamasaki, Y., Kim, C., Huang, W., Lu, S., Jhong, H. M., Gewirth, A. A., Fujigaya, T. & Nakashima, N. Insights into the Low Overpotential Electroreduction of CO_2 to CO on a Supported Gold Catalyst in an Alkaline Flow Electrolyzer. *ACS Energy Lett.* **3**, 193–198 (2018).

53. Hsieh, Y.-C., Senanayake, S. D., Zhang, Y., Xu, W. & Polyansky, D. E. Effect of Chloride Anions on the Synthesis and Enhanced Catalytic Activity of Silver Nanocoral Electrodes for CO_2 Electroreduction. *ACS Catal.* **5**, 5349–5356 (2015).

54. Nguyen, N. N., Nguyen, A. V., Steel, K. M., Dang, L. X. & Galib, M. Interfacial Gas Enrichment at Hydrophobic Surfaces and the Origin of Promotion of Gas Hydrate Formation by Hydrophobic Solid Particles. *J. Phys. Chem. C* **121**, 3830–3840 (2017).

55. Esposito, D. V. Membrane-Coated Electrocatalysts - An Alternative Approach to Achieving Stable and Tunable Electrocatalysis. *ACS Catal.* **8**, 457–465 (2018).

56. Thevenon, A., Rosas-Hernández, A., Fontani Herreros, A. M., Agapie, T. & Peters, J. C. Dramatic HER Suppression on Ag Electrodes via Molecular Films for Highly Selective CO_2 to CO Reduction. *ACS Catal.* **11**, 4530–4537 (2021).

57. Buzgar, N. & Apopei, A. THE RAMAN STUDY OF CERTAIN CARBONATES. *Analele Stiint. Univ. A.I. Cuza din Iasi* **2**, (2009).

TOC Graphic

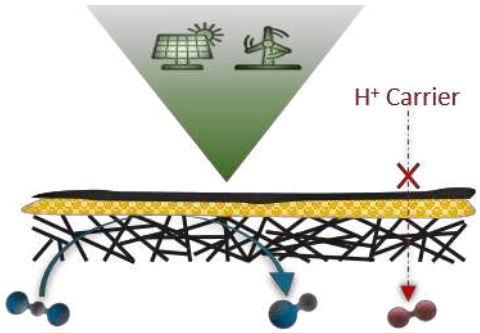

Supporting information

The Use of Nanoscale Carbon Layers on Ag-Based Gas Diffusion Electrodes to Promote CO Production

*Lien Pacquets[a,b], Järi Van den Hoek[a], Daniel Arenas-Esteban[b], Radu-George Ciocarlan[c], Pegie Cool[c], Kitty Baert[d], Tom Hauffman[d], Nick Daems[a], Sara Bals[b] and Tom Breugelmans[a]**

[a] ELCAT, University of Antwerp, Universiteitsplein 1, 2610 Wilrijk

[b] EMAT, University of Antwerp, Groenenborgerlaan 171, 2020 Antwerpen

[c] LADCA, University of Antwerp, Universiteitsplein 1, 2610 Wilrijk

[d] SURF, Vrije Universiteit Brussel, Pleinlaan 2, 1050 Brussel

*Corresponding authors: tom.breugelmans@uantwerpen.be

Lien Pacquets ORCID: 0000-0001-9457-685X

Figure S 1: Ag70Cx samples used during electrochemical experiment. Note the difference in color upon increasing the carbon layer thickness.

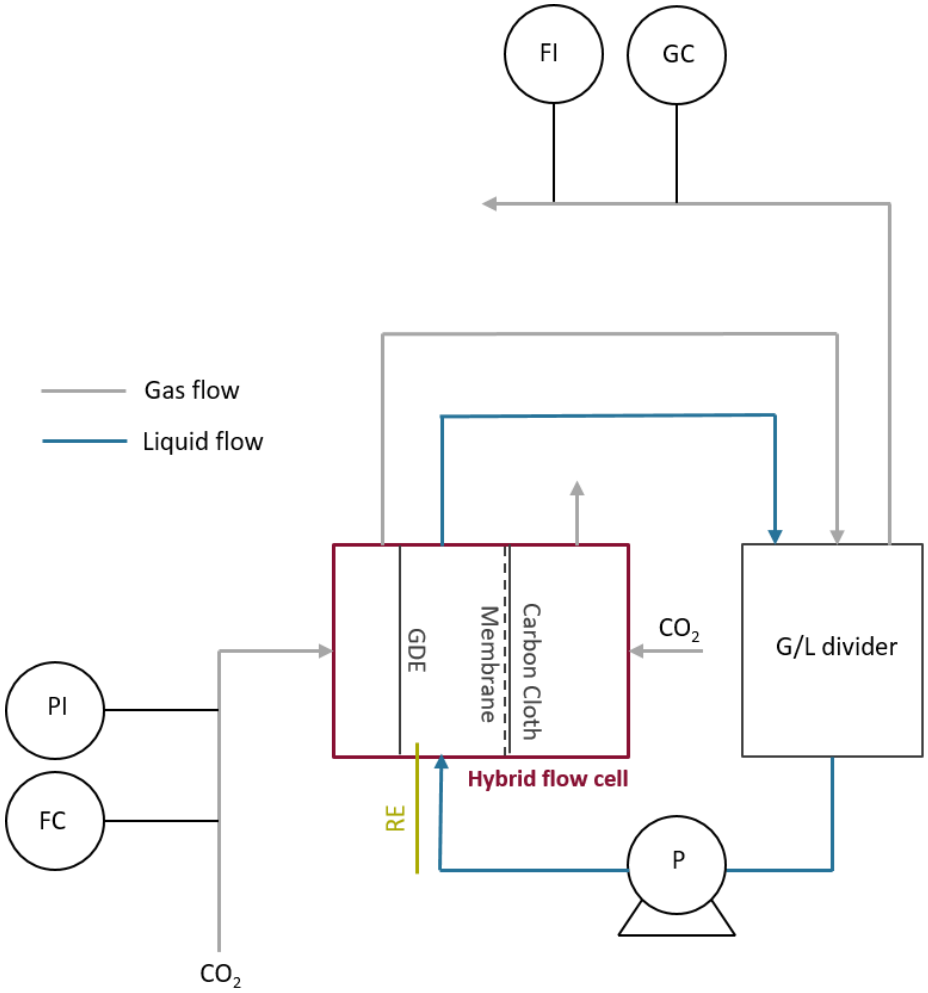

Figure S 2: Schematic representation of the hybrid flow cell. With FC being the (mass) flow controller, PI the pressure indicator, FI the (mass) flow indicator and GC the in-line gas chromatograph.

The hybrid flow cell contains three compartments which are (i) the gas channel where CO_2 is provided as feedstock; (ii) the cathode chamber which is filled with a CO_2 saturated $KHCO_3$ solution and (iii) the anolyte compartment containing a CO_2 saturated $KHCO_3$ solution. An Ag-based gas diffusion electrode (GDE) operates as the working electrode (WE) and is connected to a graphite current collector. This GDE separates the CO_2 flow from the catholyte and allows CO_2 to travel to the electrocatalyst. A carbon cloth is used as a counter electrode (CE) which is connected to an Al current collector. The CE is pressed together with the anion exchange membrane (AEM, Selemion DSVN) to reduce the ohmic resistance. The catholyte is recycled using a gas-liquid divider (G/L divider) which is also used to separate liquid from the reacted CO_2 stream and the anode compartment performs in batch mode.

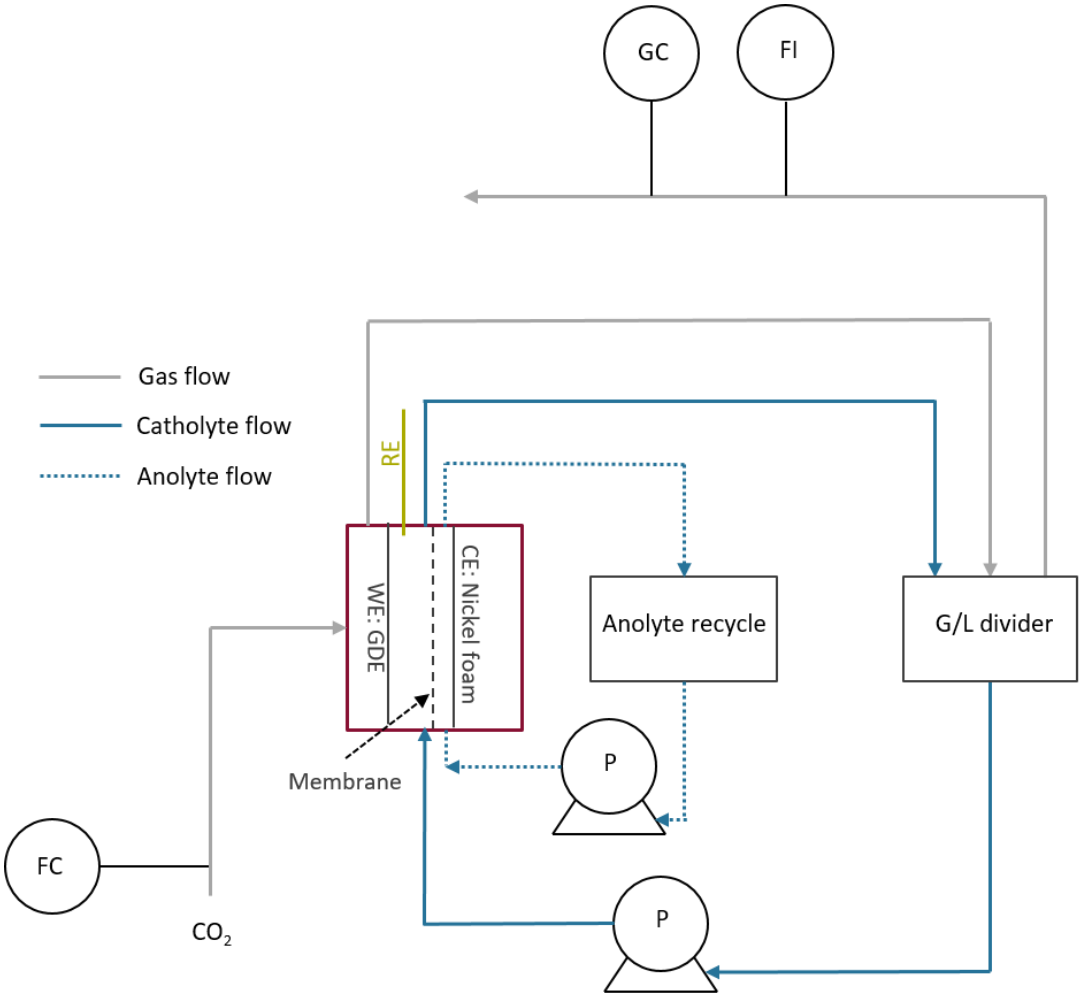

Figure S 3: Schematic representation of the flow reactor used during the durability measurements. With FC being the (mass) flow controller, FI the (mass) flow indicator and GC the in-line gas chromatograph.

This set-up has a three electrode flow-by configuration where WE and CE are separated by a cation exchange membrane (Nafion). The Ag-based GDE (WE) is connected to a copper current collector, whereas the CE consists of a nickel foam which is electrically connected to another copper current collector. A CO_2 flow is fed into the gas channel in flow-by mode and subsequently into the G/L divider before being injected into the GC to prevent liquid from entering the column of the GC. Catholyte as well as anolyte are being recycled.

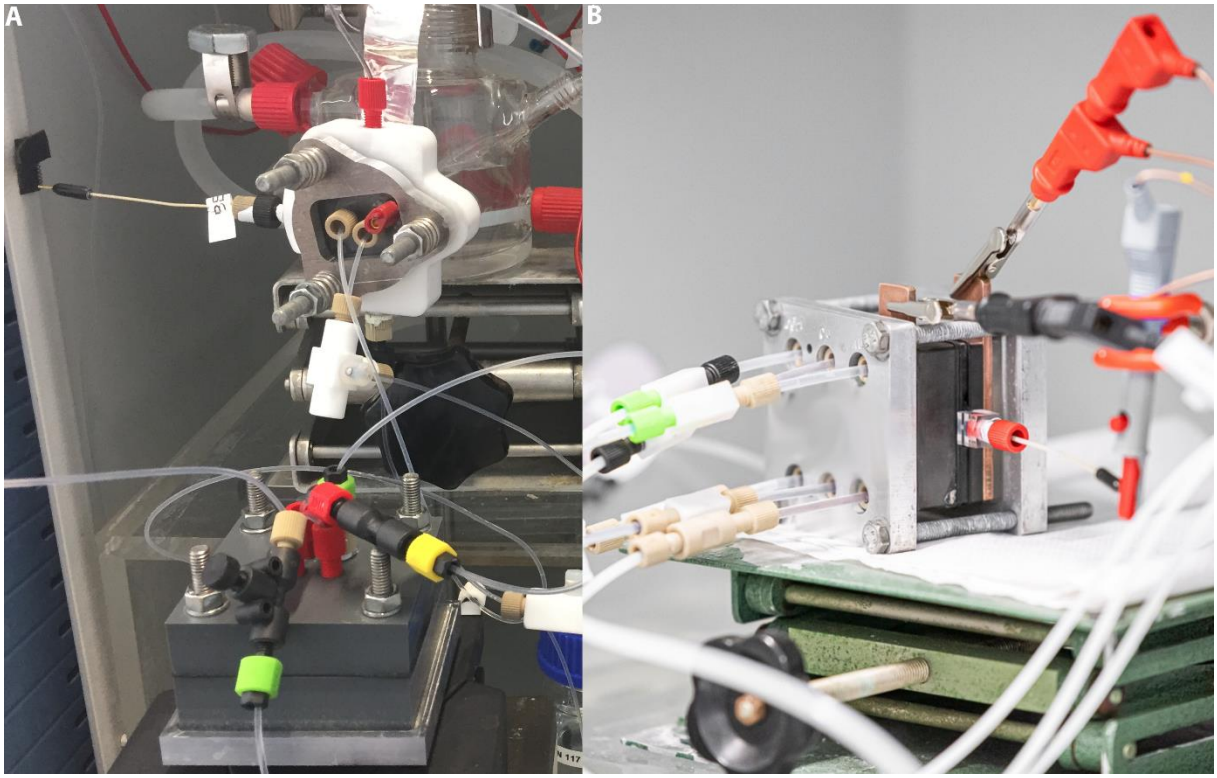

Figure S 4: Photograph of (A) the hybrid flow cell land (B) the flow reactor used for the 1 h experiment and the stability measurements, respectively.

Table S 1: Comparison of the at% of Ag and carbon between Ag-based catalysts Ag70 and Ag70C15 effecting the Ag/C ratio

Catalyst	At% Ag (%)	At% C (%)	Ag/C ratio
Ag70	3.75	84.00	0.045
Ag70C15	2.34	88.00	0.027

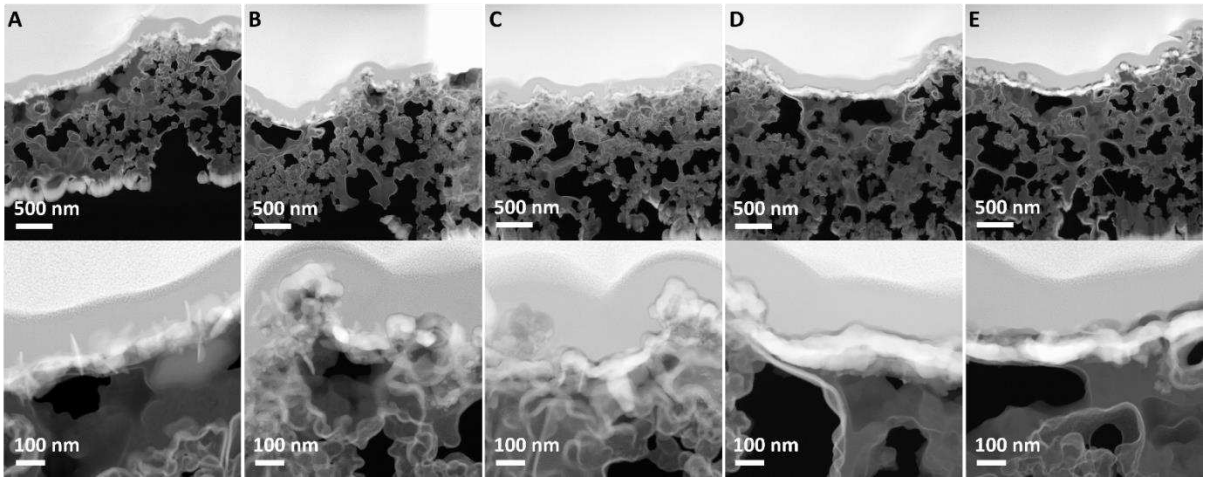

Figure S 5: (top) Low and (bottom) high magnification cross sectional HAADF STEM images of samples (A) Ag70, (B) Ag70C5, (C) Ag70C15, (D) Ag70C20 and (E) Ag70C30.

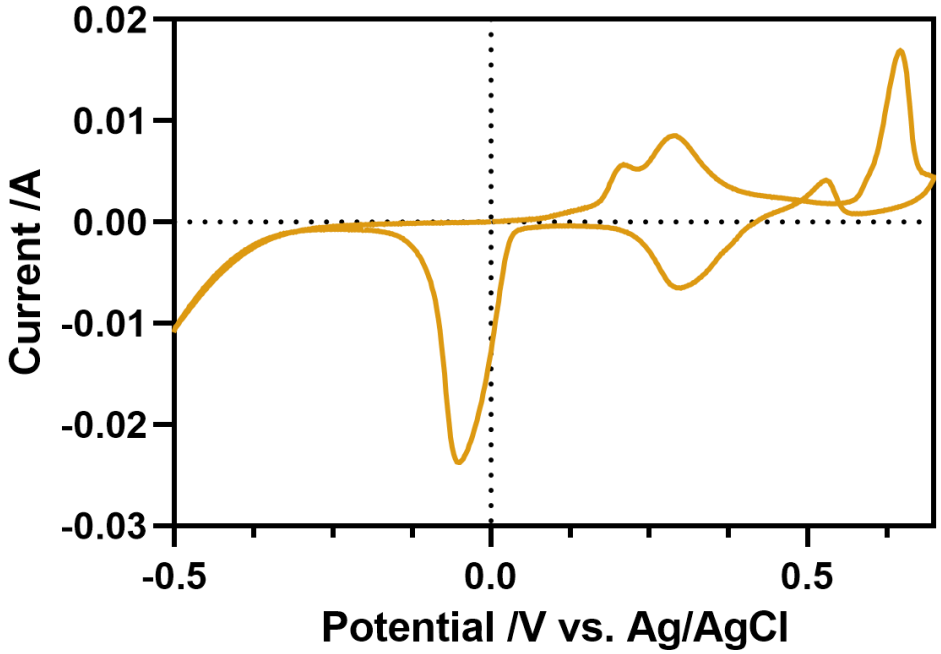

Figure S 6: CV measurement (10th scan) of Ag70C15 in 0.5 M KOH, at a scan rate of 50 mV s^{-1}

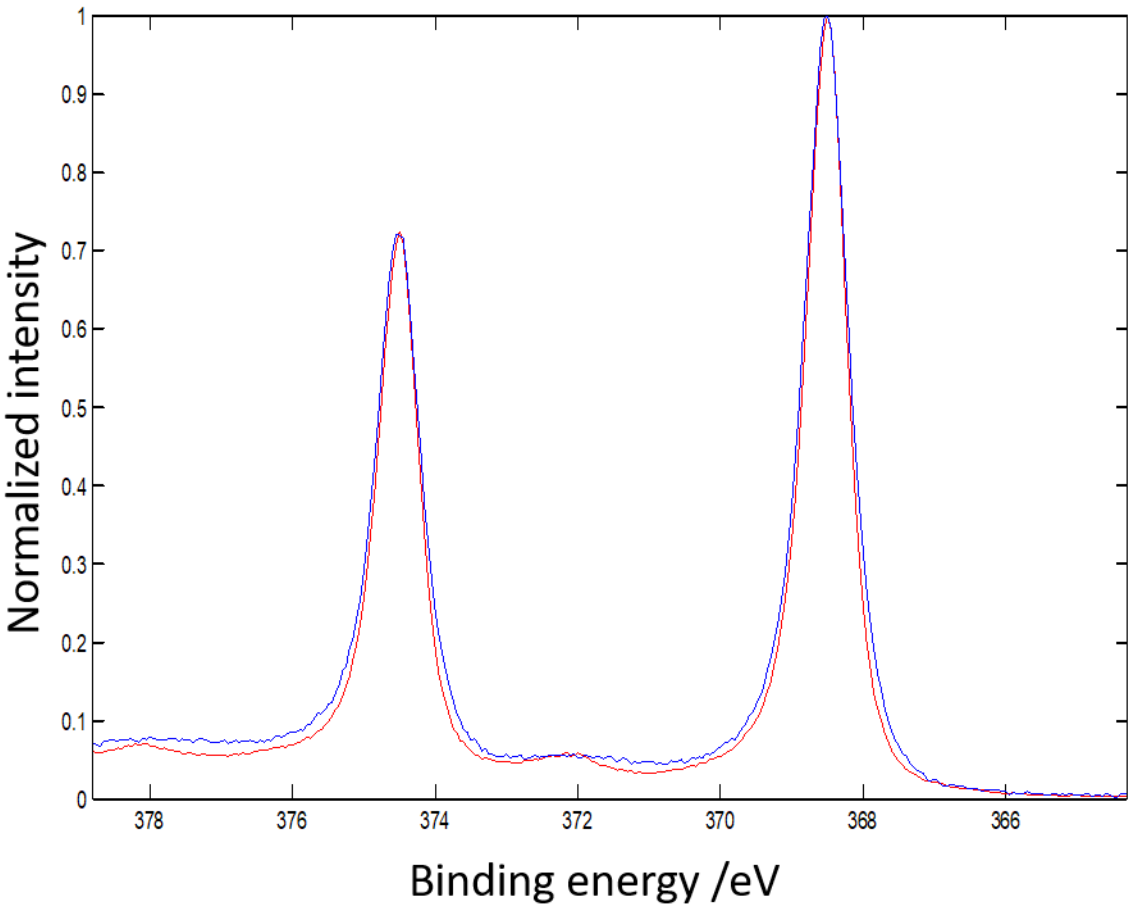

Figure S 7: Normalized high resolution spectra of Ag3d. Ag70 presented in red and Ag70C5 presented in blue.

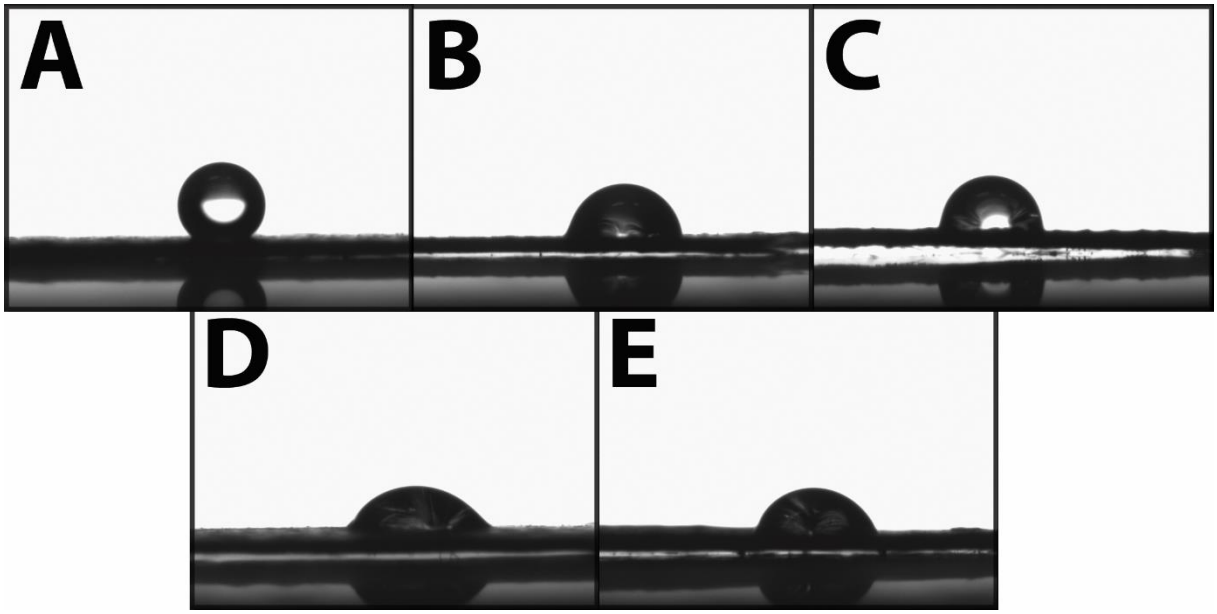

Figure S 8: Images taken during contact angle measurements of the sessile droplets of MilliQ on top of the Ag-based GDEs prior to the CO_2 reduction reaction with (A) 0 nm, (B) 5 nm, (C) 15 nm, (D) 20 nm and (E) 30 nm of carbon

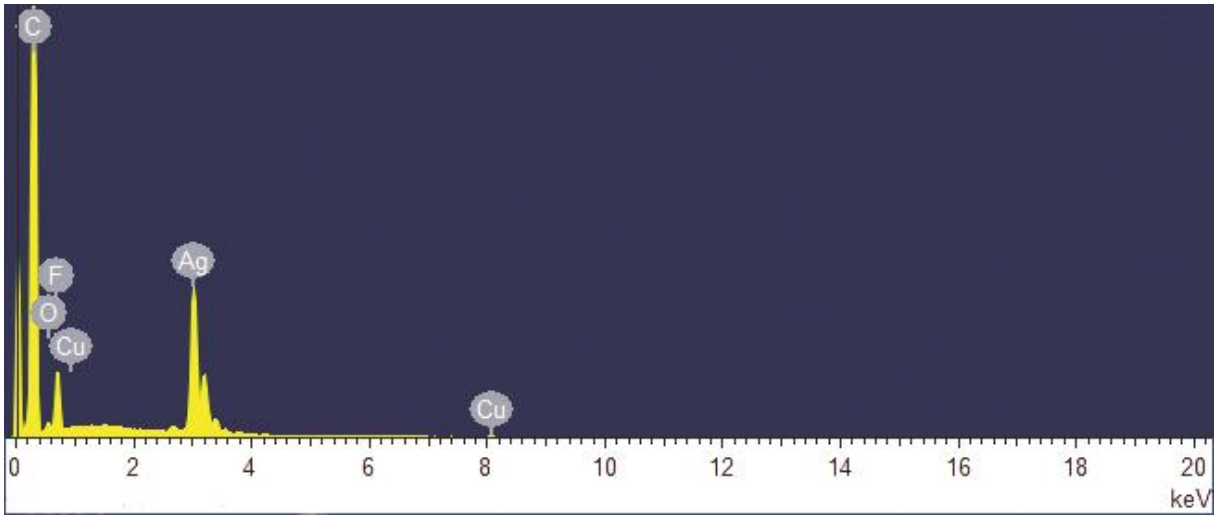

Figure S 9: EDS spectrum of the Ag70 sample depicted in Fig. 1C indicating the presence of Cu impurities inside the Ag layer

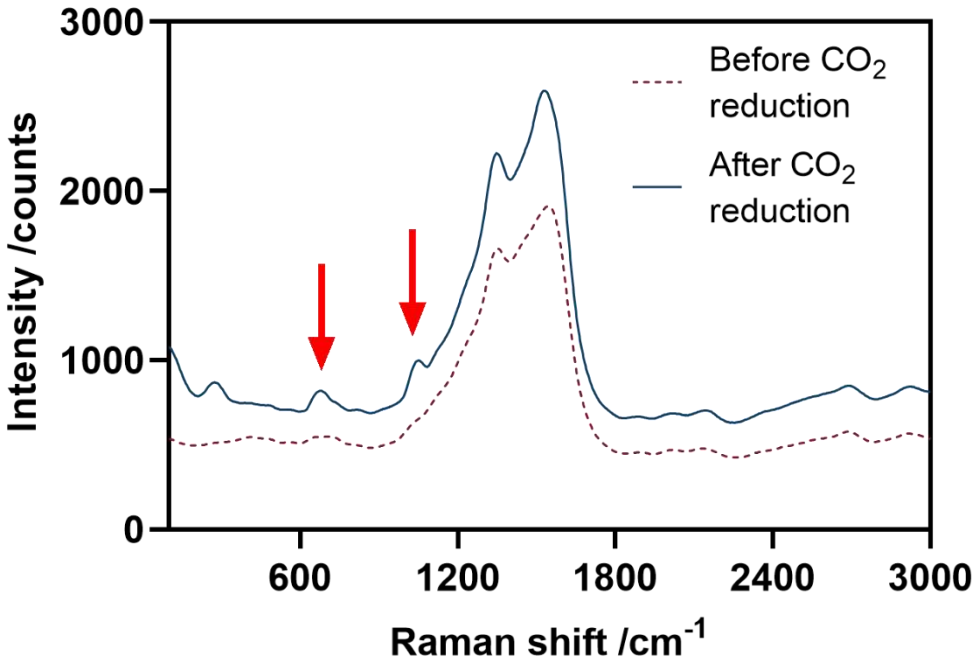

Figure S 10: Raman spectra of Ag70C20 (dashed – red) before and (solid – blue) after 1 h electrolysis